




## Spheres and fibers in turbulent flows at various Reynolds numbers

Ianto Cannon <sup>1</sup>, Stefano Olivieri <sup>1,2</sup> and Marco E. Rosti <sup>1,\*</sup>

<sup>1</sup>*Complex Fluids and Flows Unit, Okinawa Institute of Science and Technology Graduate University, 1919-1 Tancha, Onna-son, Okinawa 904-0495, Japan*

<sup>2</sup>*Department of Aerospace Engineering, Universidad Carlos III de Madrid, 28911 Leganés, Spain*



(Received 12 October 2023; accepted 3 May 2024; published 3 June 2024)

We perform fully coupled numerical simulations using immersed boundary methods of finite-size spheres and fibers suspended in a turbulent flow for a range of Taylor-Reynolds numbers  $12.8 < \text{Re}_\lambda < 442$  and solid mass fractions  $0 \leq M \leq 1$ . Both spheres and fibers reduce the turbulence intensity with respect to the single-phase flow at all Reynolds numbers, with fibers causing a more significant reduction than the spheres. The particles' effect on the anomalous dissipation tends to vanish as  $\text{Re} \rightarrow \infty$ . A scale-by-scale analysis shows that both particle shapes provide a “spectral shortcut” to the flow, but the shortcut extends further into the dissipative range in the case of fibers. Multifractal spectra of the near-particle dissipation show that spheres enhance dissipation in two-dimensional sheets, and fibers enhance the dissipation in structures with a dimension greater than one and less than two. In addition, we show that spheres suppress vortical flow structures, whereas fibers produce structures which completely overcome the turbulent vortex stretching behavior in their vicinity.

DOI: [10.1103/PhysRevFluids.9.064301](https://doi.org/10.1103/PhysRevFluids.9.064301)

### I. INTRODUCTION

Particle-laden turbulent flows abound in our environment; see, for example, volcanic ash clouds, sandstorms, and ocean microplastics. In these cases, the particles are seen in a range of shapes, and the intensity of the carrier turbulent flow can significantly vary. In this context, the present study delves into the interaction between particles and turbulent flows, focusing on two distinct particle shapes, spheres and fibers, and exploring turbulent flows across a large range of Reynolds numbers.

The interaction of particles with turbulent flows has garnered significant research attention since Richardson and Proctor [1] used balloons to track eddies in the Earth's atmosphere in 1927. Light spherical particles as tracers are now a ubiquitous experimental tool [2], and even fiber-shaped tracers have been employed [3]. For heavier particles, more complex motion is seen, such as inertial clustering [4], preferential sampling [5], and enhancement of the mean flow [6]. Numerical simulations in this field have been a valuable tool, as results can be readily processed to study length-scale-dependent statistics such as radial distribution functions [7] and histograms of Voronoi area [4]. Most of such particle-laden turbulent studies make the one-way coupling assumption, whereby the particles are affected by the fluid motion, but the fluid does not feel any effect of the particles. When the total mass fraction or volume fraction of particles in the system increases,

---

\*marco.rosti@oist.jp

Published by the American Physical Society under the terms of the [Creative Commons Attribution 4.0 International](https://creativecommons.org/licenses/by/4.0/) license. Further distribution of this work must maintain attribution to the author(s) and the published article's title, journal citation, and DOI.

the one-way coupling assumption becomes invalid, and we must model the back-reaction effect of the particles on the fluid. This opens up a zoo of new phenomena, including drag reduction [8], cluster-induced turbulence [9], and new scalings in the energy spectrum [10]. A recent review by Brandt and Coletti [11] has pointed out a gap in the current understanding of particles in turbulence, which lies between small heavy particles and large weakly buoyant particles. In addition, most real-world particle-laden flows involve particles with a high degree of anisotropy, while research in particle-laden turbulence has overwhelmingly focused on spherical particles.

This article addresses the gaps by studying a range of particle mass fractions  $M$ , ranging from single-phase ( $M = 0$ ) to fixed particles ( $M = 1$ ). We make simulations using a fully coupled approach to elucidate how particles modulate turbulence. Furthermore, we vary the turbulence intensity, allowing us to ask the question *at what Reynolds numbers ( $Re$ ) does turbulence modulation emerge? And does the modulation effect persist as  $Re \rightarrow \infty$ ?* Crucially, we connect our results to real-world flows by investigating isotropically shaped particles (spheres) and anisotropically shaped particles (fibers). The spheres have a single characteristic length, given by their diameter, whereas the fibers have two: their length and thickness. This naturally allows us to ask *how do the particle's characteristic lengths impact the scales of the turbulent flow?*

A number of works have investigated particle shape; see Voth and Soldati [12] for a review of the behavior of anisotropic particles in turbulence, including oblate spheroids, prolate spheroids and fibers. In 1932 Wadell [13] defined the sphericity of a particle as its surface area divided by the area of a sphere with equivalent volume; Wadell used sphericity to classify quartz rocks according to their shape. More recently, Zhao *et al.* [14] made direct numerical simulations of oblate and prolate spheroids in a channel flow and found that away from the channel walls, prolate spheroids tend to rotate about their symmetry axis (spinning), whereas oblate particles rotate about an axis perpendicular to their symmetry axis (tumbling). Ardekani *et al.* [15] showed that oblate spheroids can reduce drag in a turbulent channel by aligning their major axes parallel to the wall. Yousefi *et al.* [16] simulated spheres and oblate spheroids in a shear flow and found that the rotation of the spheroids can enhance the kinetic energy of the flow. At the other shape extreme from oblate spheroids, we have fibers, which are long and thin. In this article, we choose to study rigid fibers (also known as rods) as they are a simple example of a particle with high anisotropy. Concerning fibers, Paschkewitz *et al.* [17], Gillissen *et al.* [18], and others showed that rigid fibers align with vorticity in channel flows, dissipating the vortex structures, and drag reductions up to 26% have been measured [17]. In this article, we wish to investigate how the shapes and length scales of particles interact with turbulence, so we choose the triperiodic flow geometry. This geometry avoids the effects of walls and other large structures on the flow, enabling us to focus on the emergent length scales of the flow.

A few works have investigated the effect of turbulence intensity on particle-laden flows. Lucci *et al.* [19] simulated spheres of various diameters  $c$  in decaying isotropic turbulence and found that spheres reduce the fluid kinetic energy and enhance dissipation when  $c > \eta$ , where  $\eta$  is the Kolmogorov length scale. In this article, we also vary the ratio  $c/\eta$ . However, unlike [19], we do it by varying the fluid viscosity, not the particle size. This enables us to keep the particle volume, particle surface area and number of particles constant across our cases. Oka and Goto [20] studied sphere diameters in the range  $7.8 < c/\eta < 64$ , in turbulent flows with  $Re_\lambda \approx 94$ , and showed that vortex shedding and turbulence attenuation occur when  $c \gtrsim \lambda \rho / \bar{\rho}$ , where  $\lambda$  is the Taylor length scale and  $\rho$  and  $\bar{\rho}$  are the fluid and solid densities, respectively. Shen *et al.* [21] investigated the effect of solid-fluid density ratio for flows with  $38 < Re_\lambda < 74$ , and  $8.8 < c/\eta < 18$ , showing that higher-density spheres cause an increase in the normalized dissipation rate and a greater turbulence attenuation. Peng *et al.* [22] parametrized the attenuation of turbulent kinetic energy by spheres with  $7.1 < c/\eta < 15$  and  $41 < Re_\lambda < 63$ . They found that the particle mass fraction is indeed a strong indicator of attenuation, and there is negligible dependence on the Taylor-Reynolds number  $Re_\lambda$  for this range. Compared to the above works, we choose a wider range of turbulence intensities, such that  $11.7 < c/\eta < 125$  and  $12.8 < Re_\lambda < 442$ , and we extend the study to include nonspherical particles.

TABLE I. Single-phase flows.  $\text{Re}_{\text{ABC}}$  is the forcing Reynolds number, and  $M$  is the solid mass fraction. We measure the Kolmogorov length scale  $\eta \equiv \nu^{3/4}/\epsilon^{1/4}$ , the Taylor-Reynolds number  $\text{Re}_\lambda$ , and the dissipation  $\epsilon$ , which has been normalized using the integral length scale  $\mathcal{L}$  and the root mean square velocity  $u_{\text{rms}}$  of the fluid. The largest and smallest values of each parameter are shown in bold.

Marker	$\text{Re}_{\text{ABC}}$	$M$	$\eta/L$	$\text{Re}_\lambda$	$\epsilon\mathcal{L}/u_{\text{rms}}^3$
◆	<b>894</b>	<b>0.0</b>	<b><math>4.06 \times 10^{-3}</math></b>	<b>433</b>	0.399
■	447	<b>0.0</b>	$6.31 \times 10^{-3}$	308	<b>0.382</b>
▲	224	<b>0.0</b>	$1.11 \times 10^{-2}$	204	0.400
◆	112	<b>0.0</b>	$1.95 \times 10^{-2}$	116	<b>0.473</b>
●	<b>55.9</b>	<b>0.0</b>	<b><math>2.99 \times 10^{-2}</math></b>	<b>101</b>	0.428

This article is structured as follows: In the following section, we describe the numerical methods and the parameters used in our study. In Sec. III, we present and discuss the results of our simulations, and Sec. IV concludes with a summary and outlook on future research.

## II. METHODS AND SETUP

We tackle the problem using large direct numerical simulations on an Eulerian grid of  $1024^3$  points with periodic boundaries in all three directions. To obtain the fluid velocity  $u_i$  and pressure  $p$ , we solve the incompressible Navier-Stokes equations for a Newtonian fluid with kinematic viscosity  $\nu$  and density  $\rho$ ,

$$\partial_t u_i + \partial_j (u_i u_j) = \nu \partial_{jj} u_i - \partial_i p / \rho + f_i^{\text{ABC}} + f_i^{\text{sf}}, \quad (1)$$

$$\partial_j u_j = 0, \quad (2)$$

where indices  $i, j \in \{1, 2, 3\}$  denote the Cartesian components of a vector and repeated indices are implicitly summed over. The turbulent flow is sustained by an ABC forcing [23,24], which is made of sinusoids with a wavelength  $2\pi L$  equal to the domain size,

$$\begin{aligned} f_1^{\text{ABC}} &= C \sin(x_3/L) + C \cos(x_2/L), \\ f_2^{\text{ABC}} &= C \sin(x_1/L) + C \cos(x_3/L), \\ f_3^{\text{ABC}} &= C \sin(x_2/L) + C \cos(x_1/L). \end{aligned} \quad (3)$$

The amplitude  $C$  of the forcing is used to define the forcing Reynolds number  $\text{Re}_{\text{ABC}} \equiv C^{1/2} L^{3/2} / \nu$ . To discern the effect of increasing turbulence intensity, we conduct a number of simulations with various values of  $\text{Re}_{\text{ABC}}$ , given in Table I.

When the single-phase flows reach a statistically steady state, we add the solid particles at random (nonoverlapping) locations and orientations in the domain. We allow the flow to reach a statistically steady state again and measure the statistics presented in Sec. III, which were averaged in time over multiple large-eddy turnover times  $\tau_f \equiv 2\pi L / u_{\text{rms}}$ , where  $u_{\text{rms}}$  is the root mean square of the fluid velocity. This procedure is repeated for every solid mass fraction investigated, defined as  $M \equiv m_s / (m_s + m_f)$ , where  $m_s$  and  $m_f$  are the total mass of solid and fluid. The single-phase cases have  $M = 0$ , and the cases with fixed particles have  $M = 1$ . The solid phase is two-way coupled to the fluid using the immersed boundary method, and the back-reaction of the particles on the fluid is enforced by  $\mathbf{f}^{\text{sf}}$  in Eq. (1). As can be seen in Fig. 1, we simulate two types of particles, spheres and fibers; to isolate the effect of particle isotropy on the flow, we choose the fibers and spheres to have the same size: The spheres have diameter  $c$ , and the fibers have length  $c$ . We choose  $c = L/2$ , which lies inside the inertial range of scales for all of our cases.

We use the in-house Fortran code *Fujin* to solve the flow numerically. Time integration is carried out using the second-order Adams-Bashforth method, and incompressibility [Eq. (2)] is enforced

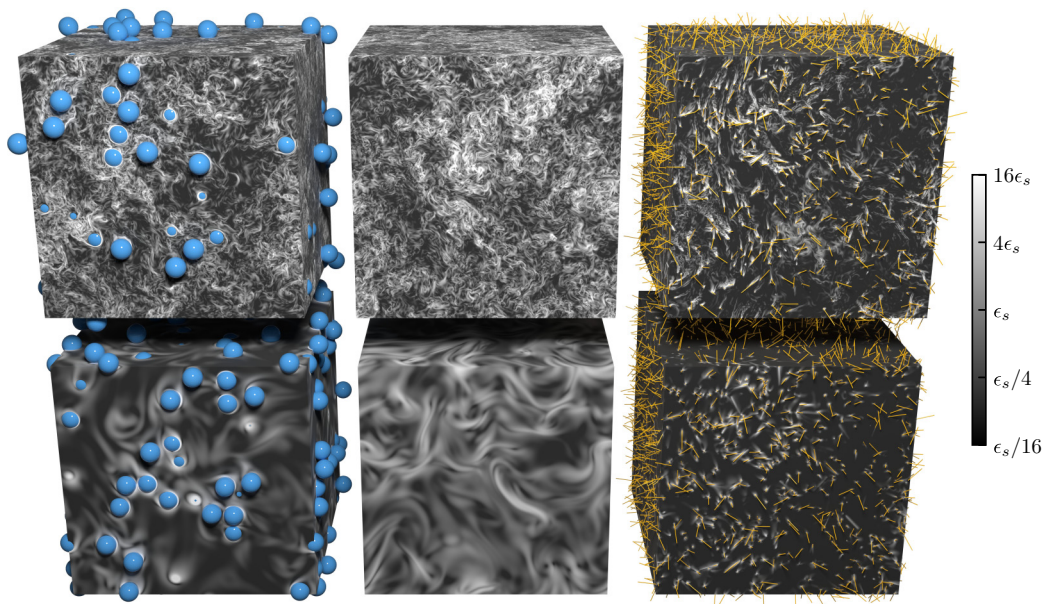


FIG. 1. Images of the simulated domain. Left column: Flows with fixed spheres. Middle column: Single-phase flows. Right column: Flows with fixed fibers. Flows on the top row have  $\text{Re}_{\text{ABC}} = 894$ . Flows on the bottom row have  $\text{Re}_{\text{ABC}} = 55.9$ . At the boundary of each domain, we show the dissipation on a logarithmic scale, where  $\epsilon_s$  is the mean dissipation of the single-phase flow at  $\text{Re}_{\text{ABC}} = 894$ .

in a pressure correction step [25], which uses the fast Fourier transform. Variables are defined on a staggered grid; velocities and forces are defined at the cell faces, while pressure is defined at the cell centers. Second-order finite differences are used for all spatial gradients [26].

### A. Motion of the spheres

The sphere motion and forces are modelled using an Eulerian-based immersed boundary method developed by Hori *et al.* [27]. The velocity  $\mathbf{U}$  and rotation rate  $\mathbf{\Omega}$  of each sphere are found by integrating the Newton-Euler equations in time

$$m\partial_t U_i = \iint_S [\rho v(\partial_i u_j + \partial_j u_i) - p\delta_{ij}] n_j dS - F^{\text{col}} n_i, \quad (4)$$

$$I\partial_t \Omega_i = \iint_S \varepsilon_{ijk} \frac{c}{2} n_j \rho v(\partial_k u_l + \partial_l u_k) n_l dS, \quad (5)$$

where  $\delta_{ij}$  is the Kronecker delta and  $\varepsilon_{ijk}$  is the Levi-Civita symbol,  $S$  is the surface of the sphere, and  $\mathbf{n}$  is its normal.  $m = \tilde{\rho}\pi c^3/6$  and  $I = mc^3/20$  are the mass and moment of inertia of the sphere with diameter  $c$  and density  $\tilde{\rho}$ . A soft-sphere collision force  $F^{\text{col}}\mathbf{n}$  is applied in the radial direction when spheres overlap [27].

Table II shows our choice of parameters for the sphere-laden flows. In all cases, we use 300 spheres, giving the solid phase a volume fraction of 0.079. The characteristic time of the spheres is  $\tau_s = \tilde{\rho}c^2/(18\rho\nu)$ , from which we can define the Stokes number  $\text{St} \equiv \tau_s/\tau_f$  of our flows. The particle Reynolds number of the spheres is  $\text{Re}_p = c\sqrt{\langle \Delta\mathbf{u}_n \cdot \Delta\mathbf{u}_n \rangle_n}/\nu$ , where  $\Delta\mathbf{u}_n$  is the difference between the velocity of the  $n$ th particle and the local fluid velocity, averaged in a ball of diameter  $2c$  centered on the sphere. The angled brackets  $\langle \cdot \rangle_n$  denote an average over all spheres in the simulation.

TABLE II. Sphere-laden flows. We set the solid-fluid density ratio  $\tilde{\rho}/\rho$  to obtain a range of solid mass fractions  $M$ . Bulk statistics for the particles are the Stokes number  $St$  and the particle Reynolds number  $Re_p$ . The largest and smallest values of each parameter are shown in bold.

Marker	$Re_{ABC}$	$M$	$\tilde{\rho}/\rho$	$\eta/L$	$Re_\lambda$	$\epsilon\mathcal{L}/u_{rms}^3$	$St$	$Re_p$
⬠	<b>894</b>	<b>0.1</b>	<b>1.29</b>	<b><math>4.09 \times 10^{-3}</math></b>	<b>431</b>	0.397	7.4	618
⬠	<b>894</b>	0.3	4.99	$4.18 \times 10^{-3}$	397	<b>0.395</b>	26.9	857
⬠	<b>894</b>	0.6	17.4	$4.09 \times 10^{-3}$	346	0.507	89.1	1120
⬠	<b>894</b>	0.9	105	$4.18 \times 10^{-3}$	280	0.625	471	1180
⬠	<b>894</b>	<b>1.0</b>	$\infty$	$4.29 \times 10^{-3}$	247	0.708	$\infty$	<b>1190</b>
■	447	<b>1.0</b>	$\infty$	$7.31 \times 10^{-3}$	161	0.786	$\infty$	559
▲	224	<b>0.1</b>	<b>1.29</b>	$1.13 \times 10^{-2}$	219	0.374	<b>1.91</b>	142
▲	224	0.3	4.99	$1.16 \times 10^{-2}$	181	0.477	6.49	198
▲	224	0.6	17.4	$1.18 \times 10^{-2}$	157	0.586	20.9	243
▲	224	0.9	105	$1.19 \times 10^{-2}$	123	0.751	109	266
▲	224	<b>1.0</b>	$\infty$	$1.26 \times 10^{-2}$	101	0.936	$\infty$	260
◆	112	<b>1.0</b>	$\infty$	$2.14 \times 10^{-2}$	61.5	1.19	$\infty$	117
●	<b>55.9</b>	<b>1.0</b>	$\infty$	<b><math>3.60 \times 10^{-2}</math></b>	<b>34.9</b>	<b>1.81</b>	$\infty$	<b>44.6</b>

### B. Motion of the fibers

For the motion and coupling of the fibers, we also use an immersed boundary method, but this one is Lagrangian and solves the Euler-Bernoulli equation for the position  $\mathbf{X}$  of the beam with coordinate  $l$  along its length [28–30]

$$\frac{\pi}{4}d^2(\tilde{\rho} - \rho)\partial_l^2 X_i = \partial_l(T\partial_l X_i) + \gamma\partial_l^4 X_i - F_i^{fs} + F_i^{col}, \quad (6)$$

where  $T$  is the tension, enforcing the inextensibility condition,

$$\partial_l X_i \partial_l X_i = 1. \quad (7)$$

The volumetric density of the fiber is  $\tilde{\rho}$  and its stiffness is  $\gamma$ . Note that the fluid density  $\rho$  in Eq. (6) cancels the inertia of the fluid in the fictitious domain inside the fiber [31]. To exclude deformation effects in our study, we choose a stiffness which limits the fiber deformation below 1%. The collision force  $\mathbf{F}^{col}$  is the minimal collision model by Snook *et al.* [32]. The fluid-solid coupling force  $\mathbf{F}^{fs}$  enacts the nonslip condition at the particle surface, and an equal and opposite force [ $\mathbf{f}^{sf}$  in Eq. (1)] acts on the fluid. The spreading kernel onto the Eulerian grid has a width of three grid spaces, giving the fiber diameter  $d = 3\Delta x$  in units of the Eulerian grid spacing [[33], equation 14]. The fiber diameter  $0.4\eta < d < 5\eta$  is on the order of the Kolmogorov length  $\eta$  in all cases, i.e., it is smaller than the turbulent eddies in the energy-containing range of the flow. This allows us to consider the fibers as infinitesimally thin objects with a high degree of anisotropy. Table III shows our choice of parameters for the fiber-laden flows. In all cases, we use  $10^4$  fibers, giving the solid phase a volume fraction of around  $5.4 \times 10^{-3}$ . The characteristic time of the fibers is calculated using a formulation which takes their aspect ratio  $\beta \equiv c/d$  into account [34],

$$\tau_s = \frac{\tilde{\rho}d^2}{18\rho\nu} \frac{\beta \ln(\beta + \sqrt{\beta^2 - 1})}{\sqrt{\beta^2 - 1}}, \quad (8)$$

from which we can define the Stokes number  $St \equiv \tau_s/\tau_f$  of our flows. The particle Reynolds number of the fibers is  $Re_p = d\sqrt{\langle \Delta \mathbf{u}_n \cdot \Delta \mathbf{u}_n \rangle_n}/\nu$ , where  $\Delta \mathbf{u}_n$  is the difference between the velocity of the midpoint of the  $n$ th fiber and the local fluid velocity, averaged in a ball of diameter  $2c$  centered on the fiber's midpoint. The angled brackets  $\langle \cdot \rangle_n$  denote an average over all fibers in the simulation.

TABLE III. Fiber-laden flows. We set the solid-fluid density ratio  $\bar{\rho}/\rho$  to obtain a range of solid mass fractions  $M$ . Bulk statistics for the particles are the Stokes number and particle Reynolds number. The largest and smallest values of each parameter are shown in bold.

Marker	$Re_{ABC}$	$M$	$\bar{\rho}/\rho$	$\eta/L$	$Re_\lambda$	$\epsilon\mathcal{L}/u_{rms}^3$	$St$	$Re_p$
⬛	<b>894</b>	0.2	47.2	$4.09 \times 10^{-3}$	422	<b>0.425</b>	1.45	34.9
⬛	<b>894</b>	0.3	81.8	<b><math>4.02 \times 10^{-3}</math></b>	<b>442</b>	0.432	2.6	41.2
⬛	<b>894</b>	0.6	279	$4.17 \times 10^{-3}$	340	0.713	7.52	46.4
⬛	<b>894</b>	0.9	1690	$4.26 \times 10^{-3}$	223	1.15	36.1	47.2
⬛	<b>894</b>	<b>1.0</b>	$\infty$	$4.40 \times 10^{-3}$	201	1.29	$\infty$	46.0
◼	447	<b>1.0</b>	$\infty$	$7.44 \times 10^{-3}$	115	1.78	$\infty$	20.6
▲	224	<b>0.1</b>	21.3	$1.16 \times 10^{-2}$	192	0.434	<b>0.155</b>	<b>8.31</b>
▲	224	0.3	81.8	$1.16 \times 10^{-2}$	196	0.465	0.605	9.9
▲	224	0.6	279	$1.19 \times 10^{-2}$	167	0.63	1.85	11.2
▲	224	0.9	1690	$1.23 \times 10^{-2}$	72.5	2.25	7.16	9.11
▲	224	<b>1.0</b>	$\infty$	$1.29 \times 10^{-2}$	54.9	3.17	$\infty$	8.22
◆	112	<b>1.0</b>	$\infty$	$2.33 \times 10^{-2}$	28.8	4.68	$\infty$	3.32
●	<b>55.9</b>	<b>1.0</b>	$\infty$	<b><math>4.27 \times 10^{-2}</math></b>	<b>12.8</b>	<b>8.60</b>	$\infty$	<b>1.51</b>

### III. RESULTS AND DISCUSSION

#### A. Bulk statistics

The Taylor-Reynolds number is defined as  $Re_\lambda \equiv u_{rms}\lambda/\nu$ , where  $u_{rms} \equiv \sqrt{\langle u_i u_i \rangle_{\mathbf{x},t}}/3$  is the root-mean-square velocity,  $\lambda = u_{rms}\sqrt{15\nu/\epsilon}$  is the Taylor length scale,  $\epsilon \equiv 2\nu\langle s_{ij}s_{ij} \rangle_{\mathbf{x},t}$  is the viscous dissipation rate,  $s_{ij} \equiv (\partial_i u_j + \partial_j u_i)/2$  is the strain-rate tensor, and angled brackets  $\langle \cdot \rangle_{\mathbf{x},t}$  indicate an average over space  $\mathbf{x}$  and time  $t$ .

The Taylor-Reynolds number is an indicator of the intensity of turbulence in the flow, and in Fig. 2, we show how  $Re_\lambda$  compares for all of our cases. Figure 2(a) shows that increasing the solid mass fraction  $M$  causes a reduction in  $Re_\lambda$  at both high and low forcing Reynolds numbers. Both spheres and fibers produce a comparable decrease in  $Re_\lambda$ , but the reduction effect is more substantial for very heavy fibers. Looking at the trend in  $Re_\lambda$  with the forcing Reynolds number  $Re_{ABC}$  in Fig. 2(b), we see, as expected, a monotonic increase in all three cases, i.e., single-phase, sphere-laden, and fiber-laden flows.

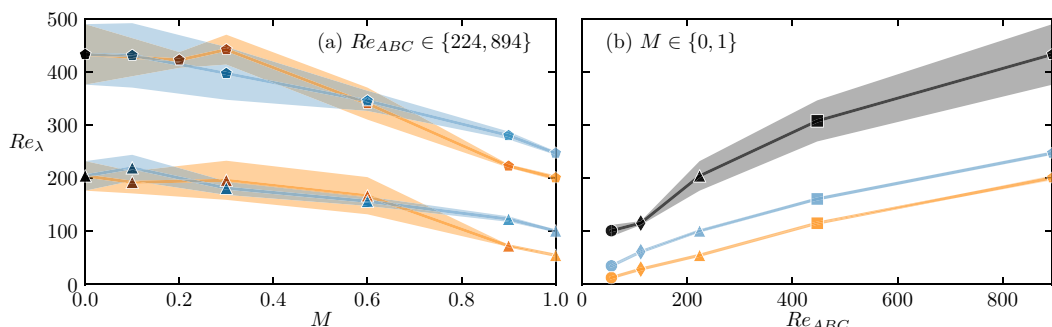


FIG. 2. (a) Effect of the solid mass fraction  $M$  on the Taylor-Reynolds number  $Re_\lambda$ . Flows with  $Re_{ABC} = 224$  are marked using triangles, and flows with  $Re_{ABC} = 894$  are marked using pentagons. (b) Effect of the forcing Reynolds number  $Re_{ABC}$  on the Taylor-Reynolds number  $Re_\lambda$  for the single-phase and particle-laden cases with fixed particles ( $M = 1$ ). In both plots, we show the single-phase flows in black, flows with spheres in blue, and flows with fibers in yellow; the shaded regions give the root mean square of  $Re_\lambda$  in time. Each case is plotted using its marker, which is listed in Tables I, II, or III.

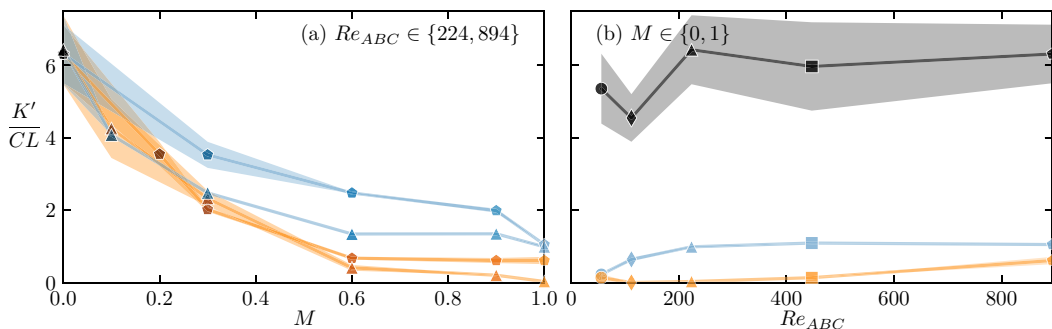


FIG. 3. The turbulent kinetic energy  $K'$ , normalized using the forcing amplitude  $C$  and length  $L$ . (a) The effect of solid mass fraction  $M$ , and (b) the effect of forcing Reynolds number  $Re_{ABC}$ . Each case is plotted using its marker, which is listed in Tables I, II, or III. We show the single-phase flows in black, flows with spheres in blue, and flows with fibers in yellow; the shaded regions give the root mean square of  $K'$  in time.

A second way to quantify turbulence is the turbulent kinetic energy  $K' \equiv \langle u'_i u'_i \rangle_{\mathbf{x},t} / 2$ . Similarly to Oka and Goto [20], we compute  $K'$  using the fluctuating part of the fluid velocity  $u'_i(\mathbf{x}, t) \equiv u_i(\mathbf{x}, t) - \langle u_i(\mathbf{x}, t) \rangle_t$ . Figure 3(a) shows the dependence of turbulent kinetic energy on particle mass fraction. We see that adding spheres and fibers reduces  $K'$  relative to the single-phase flow, with fibers having a slightly greater attenuation effect at both high and low forcing Reynolds numbers. From Fig. 3(b), we see that the turbulent kinetic energy shows only a weak dependence on  $Re_{ABC}$ , the single-phase ( $M = 0$ ) cases remain roughly constant (around  $K' \approx 6CL$ ), and flows with fixed ( $M = 1$ ) particles show a large attenuation of  $K'$  for all  $Re_{ABC}$ . This agrees with the observations of Peng *et al.* [22], who made simulations of spherical particles in homogeneous isotropic turbulence and found that the attenuation of turbulent kinetic energy has little dependence on the Reynolds number. The dissipative anomaly is a well-studied feature in single-phase turbulent flows, first proposed by Taylor [35]. It states that, even in the limit of vanishing viscosity ( $Re_\lambda \rightarrow \infty$ ), the normalized dissipation  $\epsilon \mathcal{L} / u_{\text{rms}}^3$  remains finite. The integral length scale is given by

$$\mathcal{L} = \frac{\pi}{2u_{\text{rms}}^2} \int_0^\infty \frac{E}{\kappa} d\kappa, \quad (9)$$

where  $E$  is the turbulent kinetic energy spectrum and  $\kappa$  is the wave number. In 2005, Donzis *et al.* [36] parametrized the dissipative anomaly, based on the mathematical derivation of Doering and Foias [37], they fit the function

$$\frac{\epsilon \mathcal{L}}{u_{\text{rms}}^3} = A[1 + \sqrt{1 + (B/Re_\lambda)^2}] \quad (10)$$

to a number of single-phase flows, obtaining  $A = 0.2$  and  $B = 92$ . Figure 4 shows the dependence of the normalized dissipation for our flows. We see that as  $Re_\lambda \rightarrow \infty$ , flows with spheres and fibers at all mass fractions appear to converge to the same anomalous value of dissipation  $\epsilon \mathcal{L} / u_{\text{rms}}^3 \rightarrow 0.4$ . Hence, we fit Eq. (10) with  $A = 0.2$  to each mass fraction of spheres and fibers, obtaining a value for  $B$  in each case, shown in the insets of Fig. 4. The fit to our single-phase flows agrees closely with Donzis *et al.* [36]'s result. However, both spheres and fibers cause an increase in the value of  $B$  as their mass fraction increases, with fibers producing roughly double the effect. To understand how spheres and fibers modify the dissipation in the flow, we must look at how they transport energy from large to small scales into the dissipative range.

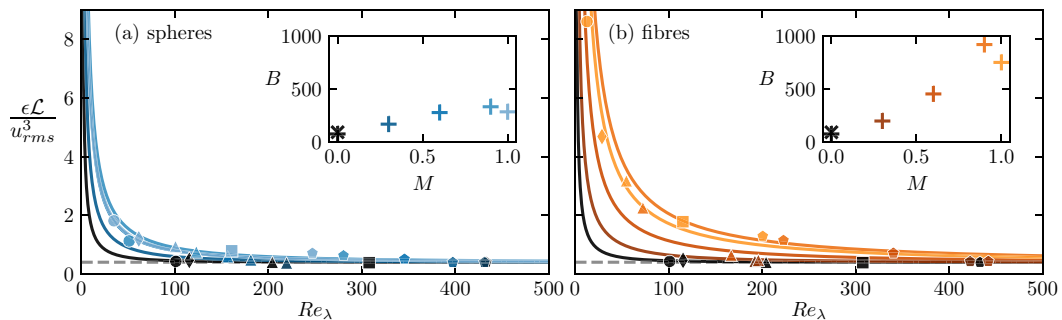


FIG. 4. The dependence of the normalized dissipation  $\epsilon \mathcal{L}/u_{rms}^3$  on the Taylor-Reynolds number  $Re_\lambda$ . Flows with spheres are in blue in panel (a), flows with fibers are in orange on panel (b), and single-phase flows are in black on both panels. Each case is plotted using its marker, which is listed in Tables I, II, or III. Dashed lines show the anomalous value of dissipation  $\epsilon \mathcal{L}/u_{rms}^3 = 0.4$  measured by Donzis *et al.* [36]. Solid lines show fits of Eq. (10) with  $A = 0.2$ . The fitted values of  $B$  are given in the inset, where Donzis' result ( $B = 92$ ) is marked with an "X."

### B. Scale-by-scale results

Figure 5 shows each flow's turbulent kinetic energy spectrum  $E$ . Single-phase flows exhibit the canonical Kolmogorov scaling  $E \sim \kappa^{-5/3}$  for one or two decades, depending on the forcing Reynolds number. Adding spheres reduces  $E$  at wave numbers up to the sphere diameter ( $\kappa < \kappa_c$ )

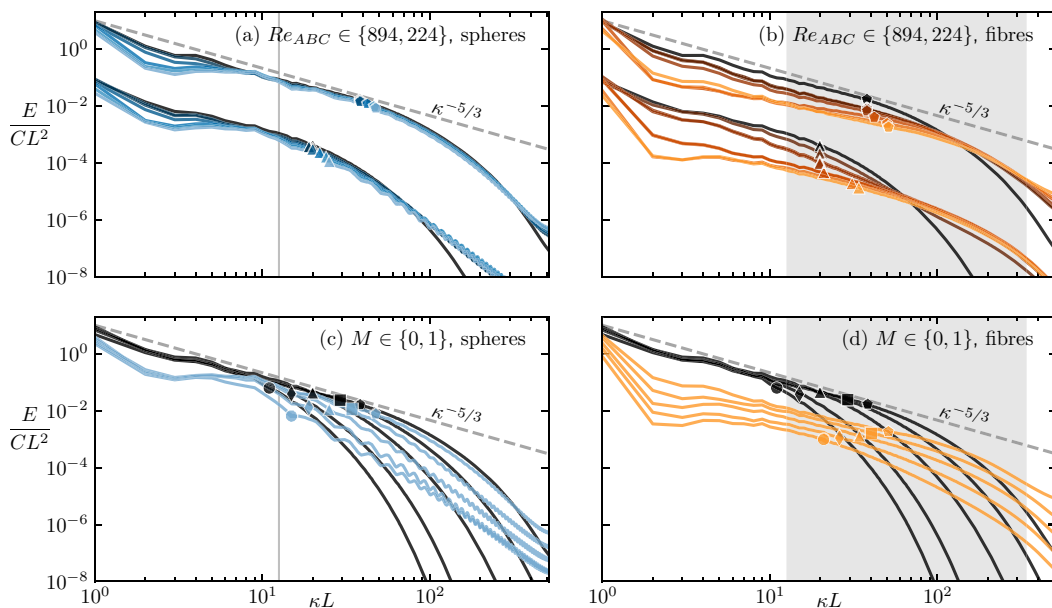


FIG. 5. Energy spectra of all cases, normalized using the forcing amplitude  $C$  and length  $L$ . On the left, we show flows with spheres, and the vertical gray lines show the wave number  $\kappa_c = 2\pi/c$  of the sphere diameter. On the right, we show flows with fibers, and we shade the region between the wave number  $\kappa_c$  of the fiber length and the wave number  $\kappa_d = 2\pi/d$  of the fiber diameter. [(a) and (b)]  $Re_{ABC} = 894$  and  $Re_{ABC} = 224$ , with the latter shifted downwards by a factor of 100 on the y axis, for various mass fractions. [(c) and (d)] Fixed ( $M = 1$ ) and single-phase ( $M = 0$ ) cases for various Reynolds numbers. Each case is marked at the wave number corresponding to the Taylor length scale, using the marker listed in Tables I, II, or III.



and increases  $E$  in the dissipative range. We mention, in passing, the oscillations at the wave number of the sphere diameter; these are an artefact resulting from the discontinuity in the velocity gradient at the sphere boundary [19]. The addition of fibers causes a reduction in  $E$  across a broad band of wavelengths ( $\kappa L \lesssim 100$ ) and a pronounced increase in the dissipative range. As was previously seen by Olivieri *et al.* [10], the energy scaling  $E \sim \kappa^{-\beta}$  becomes flatter as the mass fraction  $M$  of fibers increases. Figure 5 also shows that both spheres and fibers cause the Taylor length scale to shift to higher wave numbers due to the increase of the energy in the dissipative scales due to the presence of particles.

Figure 6 shows how each term in the Navier-Stokes equation interacts with the energy spectrum, as expressed by the spectral energy balance,

$$\mathcal{F}_{\text{inj}}(\kappa) + \Pi(\kappa) + \Pi_{\text{sf}}(\kappa) + D(\kappa) = \epsilon, \quad (11)$$

where  $\mathcal{F}_{\text{inj}}$ ,  $\Pi$ ,  $\Pi_{\text{sf}}$ , and  $D$  are the rate of energy transfer by the ABC forcing, advection, solid-fluid coupling, and dissipation, respectively. See the supplementary information of Ref. [38] for a derivation of this equation. For the single-phase flows, energy is carried by the advective term  $\Pi$  from large to small scales, where it is dissipated by the viscous term  $D$ . When particles are added, we see that the solid-fluid coupling term  $\Pi_{\text{sf}}$  acts as a ‘‘spectral shortcut’’ [10,39]; it bypasses the classical turbulent cascade, removing energy from large scales and injecting it at the length scale of the particles, through their wakes. In keeping with the spectra, the power of the solid-fluid coupling (shown by the peak value of  $\Pi_{\text{sf}}$ ) increases with mass fraction  $M$  of both spheres and fibers. For spheres, the coupling  $\Pi_{\text{sf}}$  dominates only at wave numbers less than that of the sphere diameter  $\kappa < \kappa_c$  (i.e., large length scales). Around  $\kappa_c$ , the sphere wake returns energy to the fluid, and the classical cascade resumes for  $\kappa > \kappa_c$ . For fibers instead,  $\Pi_{\text{sf}}$  extends deep into the viscous range. In fact, markers on the  $\Pi_{\text{sf}}$  curves show that spheres mostly inject energy around the length scale of their diameter, and fibers mostly inject energy at a length scale between their thickness and length. The images of dissipation in Fig. 1 support this observation; around the spheres, we see wakes comparable in size to the sphere diameter, while around the fibers, we see wakes comparable in size to the fiber thickness. We presume that the fluid-sphere coupling  $\Pi_{\text{sf}}$  would extend into the viscous range if the sphere diameter was smaller. Last, we consider the effect of Reynolds number on energy transfers in the flow, reducing  $\text{Re}_{\text{ABC}}$  limits the range of scales at which the advective flux  $\Pi$  occurs for single-phase flows. However,  $\text{Re}_{\text{ABC}}$  has little effect on the wave-number range of the solid-fluid coupling term  $\Pi_{\text{sf}}$ , suggesting that the size of the particle wakes is governed mainly by particle geometry, with a lesser effect from fluid properties like viscosity.

Moving from wave-number space to physical space, we show the longitudinal structure functions

$$S_p(r) \equiv \langle [\hat{r}_i u_i(\mathbf{x} + \mathbf{r}, t) - \hat{r}_i u_i(\mathbf{x}, t)]^p \rangle_{\mathbf{x}, \hat{\mathbf{r}}, t} \quad (12)$$

of each flow in Fig. 7, where  $\mathbf{r}$  is a separation vector between two points in the flow, it has magnitude  $r$  and direction  $\hat{\mathbf{r}}$ , and angled brackets show an average over space  $\mathbf{x}$ , direction  $\hat{\mathbf{r}}$ , and time  $t$ . For the second moment ( $p = 2$ ), the single-phase flows closely follow Kolmogorov’s scaling [40] in the inertial range ( $r \gg \eta$ ). However, when particles are added,  $S_2$  decreases relative to the single-phase case. For spheres, the decrease occurs for  $r \gtrsim c$ , while for fibers, it occurs at even smaller separations  $r$ . Much like the  $E \sim k^{-\beta}$  scalings seen in Fig. 5, the decreased regions in Fig. 7 show scalings  $S_2 \sim r^{\zeta_2}$ , which become flatter for larger mass fractions  $M$ . These energy spectrum and structure-function scalings are, in fact, just observations of the same phenomenon, as the exponents are related by  $\zeta_2 = \beta - 1$  for any differentiable velocity field [[41], p. 232]. In the higher moment structure function ( $p = 6$ ), the flattening of the  $S_6 \sim r^{\zeta_6}$  scaling by the particles is yet more apparent, indicating that the tails of the probability distribution of  $\hat{r}_i u_i(\mathbf{x} + \mathbf{r}) - \hat{r}_i u_i(\mathbf{x})$  become wider for smaller separations  $r$ . In other words, extreme values become more common, and the velocity field becomes more intermittent in space. In the case of single-phase homogeneous-isotropic turbulence, the intermittency of the velocity field has been linked to the non-space-filling nature of the fluid dissipation [42]. Next, we explore this link in the case of particle-laden turbulence by investigating the intermittency of dissipation  $\epsilon$  in space.

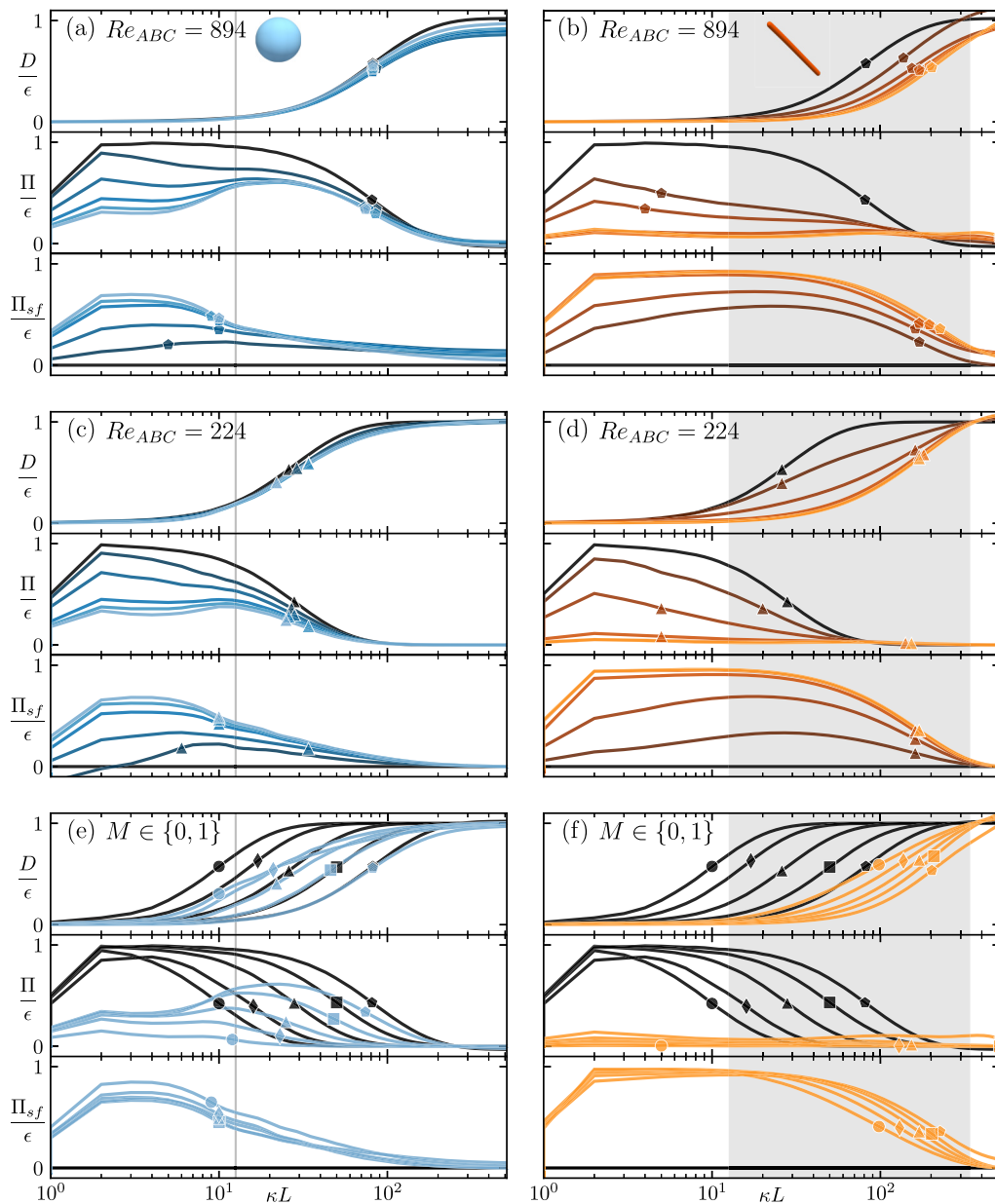


FIG. 6. Scale-by-scale energy balance for all cases. [(a) and (b)]  $Re_{ABC} = 894$  cases for various mass fractions. [(c) and (d)]  $Re_{ABC} = 224$  cases for various mass fractions. [(e) and (f)] Fixed ( $M = 1$ ) and single-phase ( $M = 0$ ) cases for various Reynolds numbers. On the left, we show flows with spheres, and the vertical gray lines show the wave number  $\kappa_c = 2\pi/c$  of the sphere diameter. On the right, we show flows with fibers, and we shade the region between the wave number  $\kappa_c$  of the fiber length and the wave number  $\kappa_d$  of the fiber diameter. For each case, we plot three terms: the dissipation  $D$ , the energy flux  $\Pi$  due to convection, and the energy flux  $\Pi_{sf}$  due to the solid-fluid coupling. Each curve is marked where the gradient is largest, using the marker listed in Tables I, II, or III.

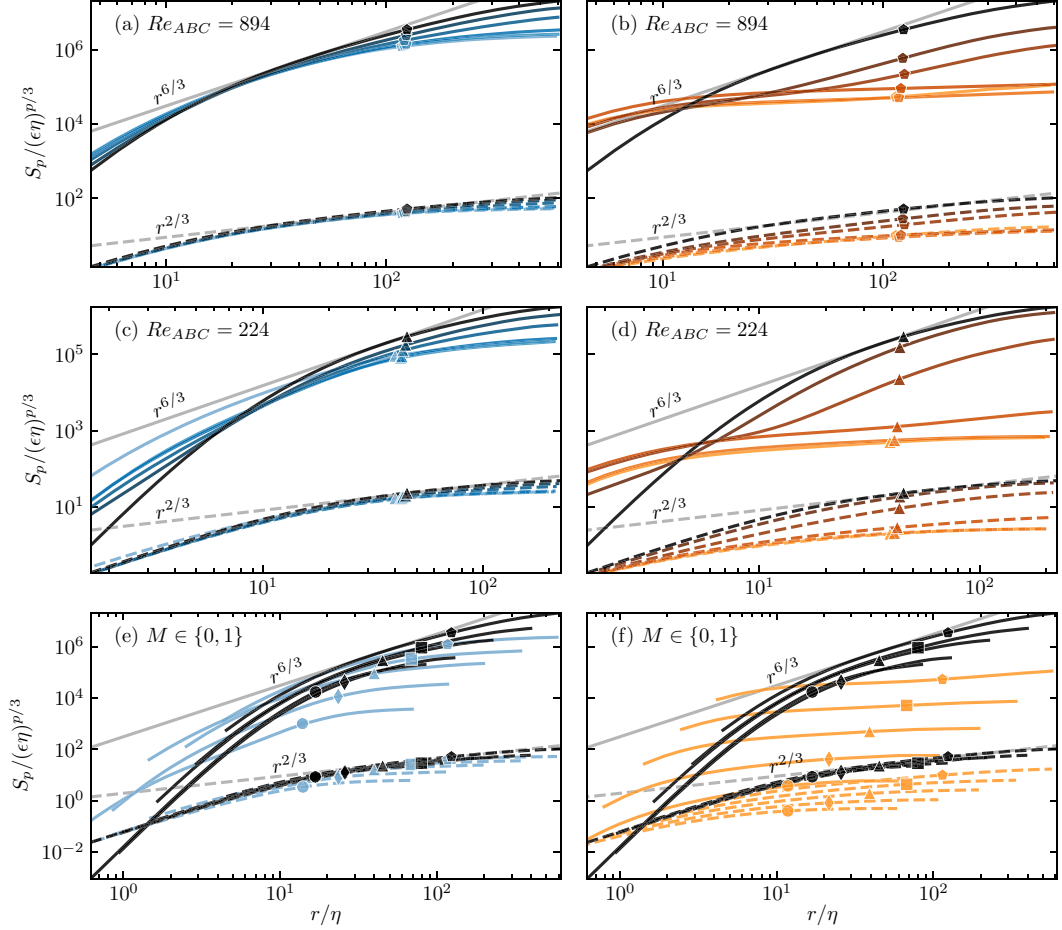


FIG. 7. Structure functions of order  $p = 2$  (dashed lines) and  $p = 6$  (solid lines). [(a) and (b)] Cases with  $Re_{ABC} = 894$  for various mass fractions. [(c) and (d)] Cases with  $Re_{ABC} = 224$  for various mass fractions. [(e) and (f)] Fixed ( $M = 1$ ) and single-phase ( $M = 0$ ) cases for various Reynolds numbers. Flows with spheres are on the left, and flows with fibers are on the right. Gray lines show the scalings predicted by Kolmogorov [40] for the single-phase structure functions. We mark each line at  $r = c$  using the marker listed in Tables I, II, or III.

Using the method described by Frisch [[42], p. 159], Meneveau and Sreenivasan [43], and others, we obtain the quantity  $\epsilon_l$  by averaging the viscous dissipation within a spherical region of radius  $l$  (hereafter, we refer to this averaging region as a “ball” to avoid confusion with the particles). To observe the variation of  $\epsilon_l$  we take its square and average over many balls of radius  $l$  at different locations and times, where this average is denoted using angled brackets  $\langle \cdot \rangle$ . Figure 8 shows how  $\langle \epsilon_l^2 \rangle$  depends on the radius  $l$  of the balls. At large radii ( $l \rightarrow \infty$ ),  $\epsilon_l$  is by definition equivalent to the bulk value  $\epsilon$ , and so  $\langle \epsilon_l^2 \rangle / \epsilon^2$  tends to unity. However, for  $l < L$ , we see that  $\langle \epsilon_l^2 \rangle / \epsilon^2 > 1$  in all of the cases plotted. This increase indicates that there are localized regions of high dissipation in the fluid. In other words, the dissipation fields are intermittent in space. For the single-phase flows,  $\langle \epsilon_l^2 \rangle$  reaches a plateau for  $l < \eta$ , giving an indication of the size of these flow structures. For the sphere-laden flows, we see that  $\langle \epsilon_l^2 \rangle$  reaches almost 100 times the bulk value and remains roughly constant for small radii ( $l < 0.05L$ ). This suggests that the spherical particles are creating high-dissipation structures in the fluid, and balls with  $l < 0.05L$  fit entirely inside these structures.

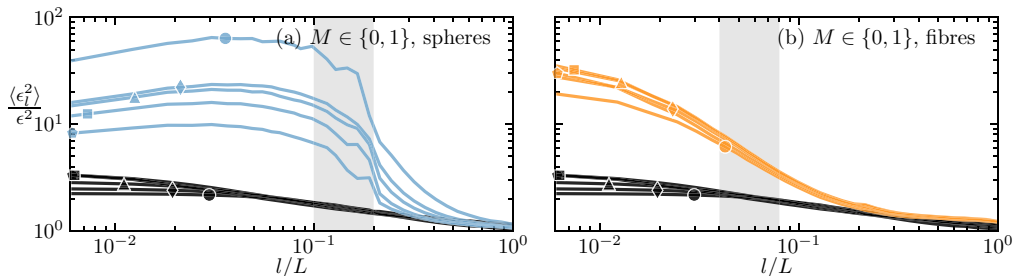


FIG. 8. The fluid dissipation averaged in balls of radius  $l$  and squared. We mark each case at  $l = \eta$  using the marker listed in Tables I, II, or III. We shade the regions where  $\langle \epsilon_l^2 \rangle$  shows a strong dependence on  $l$ , for sphere-laden flows (a) this is  $0.1L \leq l \leq 0.2L$ , whereas for fiber-laden flows (b) this is  $0.04L \leq l \leq 0.08L$ .

That is, reducing the ball radius below  $l = 0.05L$  has minimal effect on  $\langle \epsilon_l^2 \rangle$  because the majority of balls are sampling either entirely inside a high-dissipation structure or entirely outside. In the case of fibers, high-dissipation structures also produce an increase in  $\langle \epsilon_l^2 \rangle$  for small  $l$ ; here no plateau is seen, implying that even the smallest balls ( $l = 6 \times 10^{-3}L$ ) cannot fit inside the high-dissipation structures created by the fibers.

To measure the fractal dimension of the high-dissipation structures, we take a range of moments  $-6 \leq q \leq 6$  of  $\epsilon_l$ . This quantity has a scaling behavior

$$\langle \epsilon_l^q \rangle \sim l^\tau, \quad (13)$$

if the dissipation field is multifractal [42]. Indeed, for the sphere-laden flows in Fig. 8(a),  $\langle \epsilon_l^2 \rangle$  has a strong dependence on  $l$  in the range  $0.1L \leq l \leq 0.2L$ , and for the fiber-laden flows in Fig. 8(b),  $\langle \epsilon_l^2 \rangle$  has a strong dependence on  $l$  in the range  $0.04L \leq l \leq 0.08L$ . Hence, we calculate  $\tau$  by making lines of best fit in these ranges, and we obtain the multifractal spectra  $F(\alpha)$  with a Legendre transformation,

$$\alpha = \frac{d\tau}{dq} + 1, \quad (14)$$

$$F = q(\alpha - 1) - \tau + 3. \quad (15)$$

Figure 9 shows the multifractal spectra for all cases. Similarly to Mukherjee *et al.* [44], we split our analysis into separate regions: Solid curves result from an ensemble average over balls not containing particles, while dashed curves result from an ensemble average over balls containing particles. We see that the multifractal spectra of the single-phase flows and the regions not containing particles have peaks at  $\alpha \approx 1$ ,  $F \approx 3$ , showing there is a background of space-filling dissipation in these regions [[42], p. 163]. In addition, the presence of tails in the spectra shows that the dissipation fields are not self-similar and violate the hypotheses made by Kolmogorov [40] for a turbulent flow. This can explain the flattening of the high-order structure functions ( $S_6$  in Fig. 7) relative to Kolmogorov's predictions. We note in passing that the single-phase flows with lower Reynolds number ( $\text{Re}_{\text{ABC}} = 55.9$  and  $\text{Re}_{\text{ABC}} = 112$ ) show narrower tails in Fig. 9(f), as viscous effects are present here.

The multifractal spectra of the regions containing spheres (blue dashed lines in Fig. 9) have peaks which are shifted to the left. This shift can be explained by considering the high dissipation in the boundary layers around the spheres. As imaged in Fig. 12, the boundary layers have a higher dissipation rate than the surrounding fluid and are confined in space to relatively thin sheets. In Fig. 9(e) we sketch a ball of radius  $l$  intersecting with a sphere's boundary layer which has thickness  $\delta \ll l$ . The volume of the high-dissipation region inside the ball is  $\pi l^2 \delta$ , and hence the

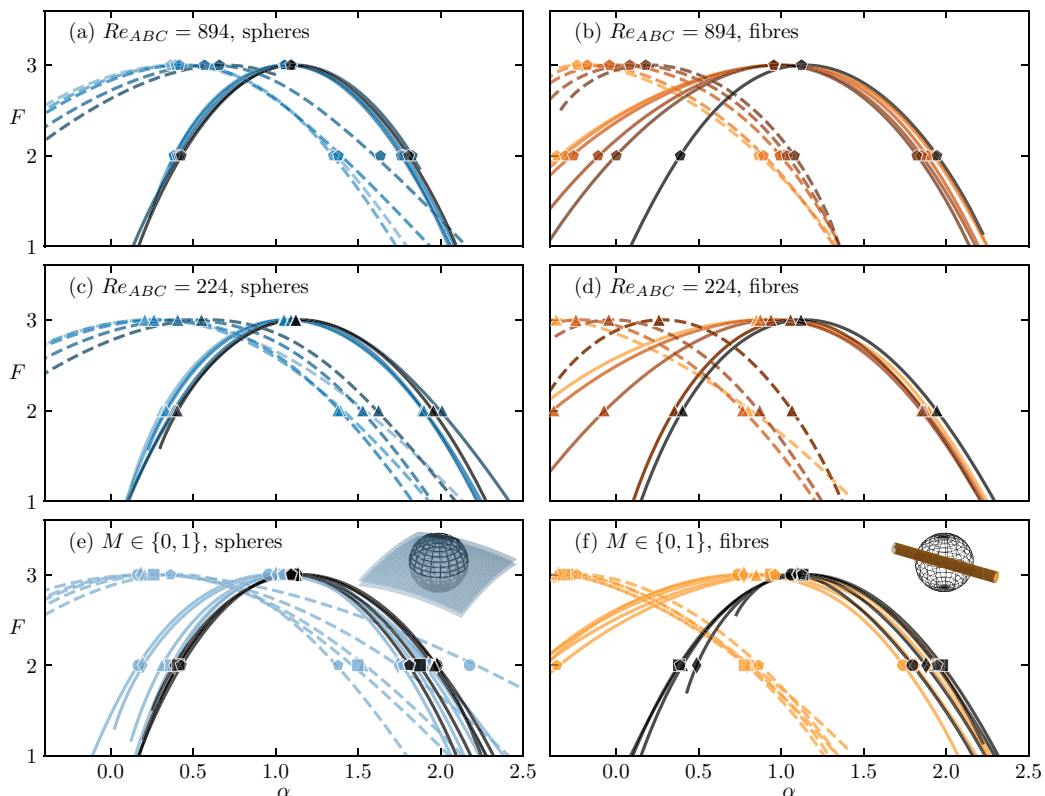


FIG. 9. Multifractal spectra of the dissipation in regions containing particles (dashed lines) and regions not containing particles (solid lines). Spectra in the left panels [(a), (c), and (e)] were calculated using balls of radius  $0.1L \leq l \leq 0.2L$ . Spectra in the right panels [(b), (d), and (f)] were calculated using balls of radius  $0.04L \leq l \leq 0.08L$ . We mark each line case where  $F$  is maximum and at  $F = 2$  using the marker listed in Tables I, II, or III. [(a) and (b)] Cases with  $Re_{ABC} = 894$  for various mass fractions. [(c) and (d)] Cases with  $Re_{ABC} = 224$  for various mass fractions. [(e) and (f)] Fixed ( $M = 1$ ) and single-phase ( $M = 0$ ) cases for various Reynolds numbers. [(e), inset] A two-dimensional sheet intersecting with a ball, and [(f), inset] a one-dimensional tube intersecting with a ball.

total dissipation in the ball roughly scales as  $\sim l^2$ . When we average over the volume of the ball ( $4\pi l^3/3$ ) and take the  $q$ th moment, we obtain  $\langle \epsilon_l^q \rangle \sim l^{2q} l^{-3q}$ . Comparing with Eq. (13), this scales as  $\tau = -q$ . Applying a Legendre transformation [Eqs. (14) and (15)] this corresponds to the point  $\alpha = 0, F = 3$ , which is roughly where we find the peaks in the multifractal spectra of the regions containing spheres. This reinforces our observation that the dissipation in the regions around the spherical particles is confined to sheetlike structures.

The multifractal spectra of the regions containing fibers (orange dashed lines in Fig. 9) have peaks which are shifted even further to the left. Again, we explain this by considering the boundary layers around the particles. In Fig. 9(f) we sketch a ball of radius  $l$  intersecting with a fiber's boundary layer which has radius  $\delta \ll l$ . In this case, the volume of the high-dissipation region is  $\pi \delta^2 l$ . Thus, the average dissipation in the ball scales as  $\langle \epsilon_l^q \rangle \sim l^q l^{-3q}$ , so the resulting scaling is  $\tau = -2q$ , which [by Eqs. (14) and (15)] corresponds to the point  $\alpha = -1, F = 3$ . In fact, in Fig. 9(f), we see that the ensemble average over balls containing  $M = 1$  fibers produces peaks around  $\alpha = -0.5$ , suggesting that the wakes around the fibers are not exactly thin tubes, but more space-filling structures with a

fractal dimension between one and two. This is also supported by the images in Fig. 12, as wakes are seen to extend behind the fibers.

The middle and upper panels of Fig. 9 show that (at  $\text{Re}_{\text{ABC}} = 224$  and  $\text{Re}_{\text{ABC}} = 894$ ) the sphere- and fiber-containing multifractal spectra tend toward the single-phase multifractal spectrum as  $M$  is reduced. This is expected as the particle-fluid relative velocity is reduced and the wakes become less prominent compared to the background space-filling turbulence. On the other hand, the ensembles of balls not containing particles produce multifractal spectra with low  $\alpha$  tails that extend beyond those of the single-phase multifractal spectra, suggesting that the wakes of spheres and fibers extend into the bulk of the fluid and that they retain their non-space-filling nature.

### C. Local flow structures

To look more closely at the flow structures produced by the particles, we compute the alignment of the unit-length eigenvectors  $\hat{\mathbf{a}}_1$ ,  $\hat{\mathbf{a}}_2$ , and  $\hat{\mathbf{a}}_3$  of the strain-rate tensor  $s_{ij} \equiv (\partial_i u_j + \partial_j u_i)/2$  with the vorticity  $\boldsymbol{\omega} \equiv \varepsilon_{ijk} \partial_j u_k \hat{\mathbf{e}}_i$  [45,46], where  $\hat{\mathbf{e}}_1$ ,  $\hat{\mathbf{e}}_2$ , and  $\hat{\mathbf{e}}_3$  are the Cartesian unit vectors and  $\varepsilon_{ijk}$  is the Levi-Civita symbol. We choose  $\hat{\mathbf{a}}_1$  to be the eigenvector corresponding to the largest eigenvalue. For an incompressible fluid, the three eigenvalues of  $s_{ij}$  sum to zero, so the largest eigenvalue is never negative. Hence,  $\hat{\mathbf{a}}_1$  aligns with the direction of elongation in the flow. Similarly, we choose the eigenvector  $\hat{\mathbf{a}}_3$  to correspond with the smallest eigenvalue, which is never positive, so  $\hat{\mathbf{a}}_3$  aligns with the direction of compression in the flow. Finally, due to the symmetry of the strain-rate tensor,  $\hat{\mathbf{a}}_2$  is orthogonal to the other two eigenvectors and, depending on the flow, there can be compression or elongation along its axis. Figure 10 shows probability-density functions  $P$  of the scalar product of the unit-length vorticity  $\hat{\boldsymbol{\omega}}$  with  $\hat{\mathbf{a}}_1$ ,  $\hat{\mathbf{a}}_2$  and  $\hat{\mathbf{a}}_3$  for all of the flows studied. The quantity  $\hat{\boldsymbol{\omega}} \cdot \hat{\mathbf{a}}_i$  is simply the cosine of the angle between the two vectors, and we take the modulus because  $\hat{\mathbf{a}}_i$  and  $-\hat{\mathbf{a}}_i$  are degenerate eigenvectors. In the single-phase flows,  $P$  is maximum at  $|\hat{\boldsymbol{\omega}} \cdot \hat{\mathbf{a}}_2| = 1$ , that is, we see a strong alignment of vorticity with the intermediate eigenvector  $\hat{\mathbf{a}}_2$ . This is a well-known feature of turbulent flows and has been attributed to the axial stretching of vortices [45]. Also in keeping with previous observations of single-phase turbulence, we see that the first eigenvector  $\hat{\mathbf{a}}_1$  shows very little correlation with  $\hat{\boldsymbol{\omega}}$ , and the last eigenvector is mostly perpendicular to the vorticity, producing a peak in  $P$  at  $\hat{\boldsymbol{\omega}} \cdot \hat{\mathbf{a}}_3 = 0$ . When spheres are added, vorticity aligns even more strongly with the intermediate eigenvector  $\hat{\mathbf{a}}_2$  and becomes more perpendicular to the first and last eigenvectors  $\hat{\mathbf{a}}_1$  and  $\hat{\mathbf{a}}_3$ . This change is consistent with the existence of a shear layer at the surface of the spheres or in the wakes behind the spheres. To demonstrate this, we draw a laminar shearing flow and label the directions of  $\hat{\mathbf{a}}_1$ ,  $\hat{\mathbf{a}}_2$ ,  $\hat{\mathbf{a}}_3$ , and  $\hat{\boldsymbol{\omega}}$  in the inset of Fig. 10. The compression  $\hat{\mathbf{a}}_3$  and extension  $\hat{\mathbf{a}}_1$  are in the plane of the shear flow, while the vorticity  $\hat{\boldsymbol{\omega}}$  and the intermediate eigenvector  $\hat{\mathbf{a}}_2$  are perpendicular to the shear plane; this gives rise to the  $\hat{\boldsymbol{\omega}} \cdot \hat{\mathbf{a}}_1 = 0$ ,  $|\hat{\boldsymbol{\omega}} \cdot \hat{\mathbf{a}}_2| = 1$ , and  $\hat{\boldsymbol{\omega}} \cdot \hat{\mathbf{a}}_3 = 0$  modes in the sphere-laden flows in Fig. 10. The larger mass fraction spheres have a greater effect, as their motion relative to the fluid is larger. Also, the spheres' effect is more pronounced at lower  $\text{Re}_{\text{ABC}}$ , which can be explained by an increased thickness in the shear layer as the fluid viscosity increases. For fiber-laden flows, peaks are also seen at  $\hat{\boldsymbol{\omega}} \cdot \hat{\mathbf{a}}_1 = 0$ ,  $|\hat{\boldsymbol{\omega}} \cdot \hat{\mathbf{a}}_2| = 1$ , and  $\hat{\boldsymbol{\omega}} \cdot \hat{\mathbf{a}}_3 = 0$ , but the peaks are spread over a larger range of angles, presumably due to the high curvature of the fiber surfaces, which adds variance to the local direction of vorticity and shear. At small Reynolds numbers ( $\text{Re}_{\text{ABC}} = 55.9$  and 112) the peaks are widest and  $P(|\hat{\boldsymbol{\omega}} \cdot \hat{\mathbf{a}}_i|)$  becomes an almost uniform distribution.

The local topology of a flow can be described entirely using the three principle invariants of the velocity gradient tensor  $\partial_i u_j$  [47]. The first invariant  $\partial_i u_i$  is not interesting in our case because it is zero for an incompressible fluid. However, the second invariant,

$$Q = \frac{1}{4} \omega_i \omega_i - \frac{1}{2} s_{ij} s_{ij}, \quad (16)$$

expresses the balance of vorticity and strain, while the third invariant,

$$R = \frac{1}{4} \omega_i s_{ij} \omega_j - \frac{1}{3} s_{ij} s_{jk} s_{ki}, \quad (17)$$

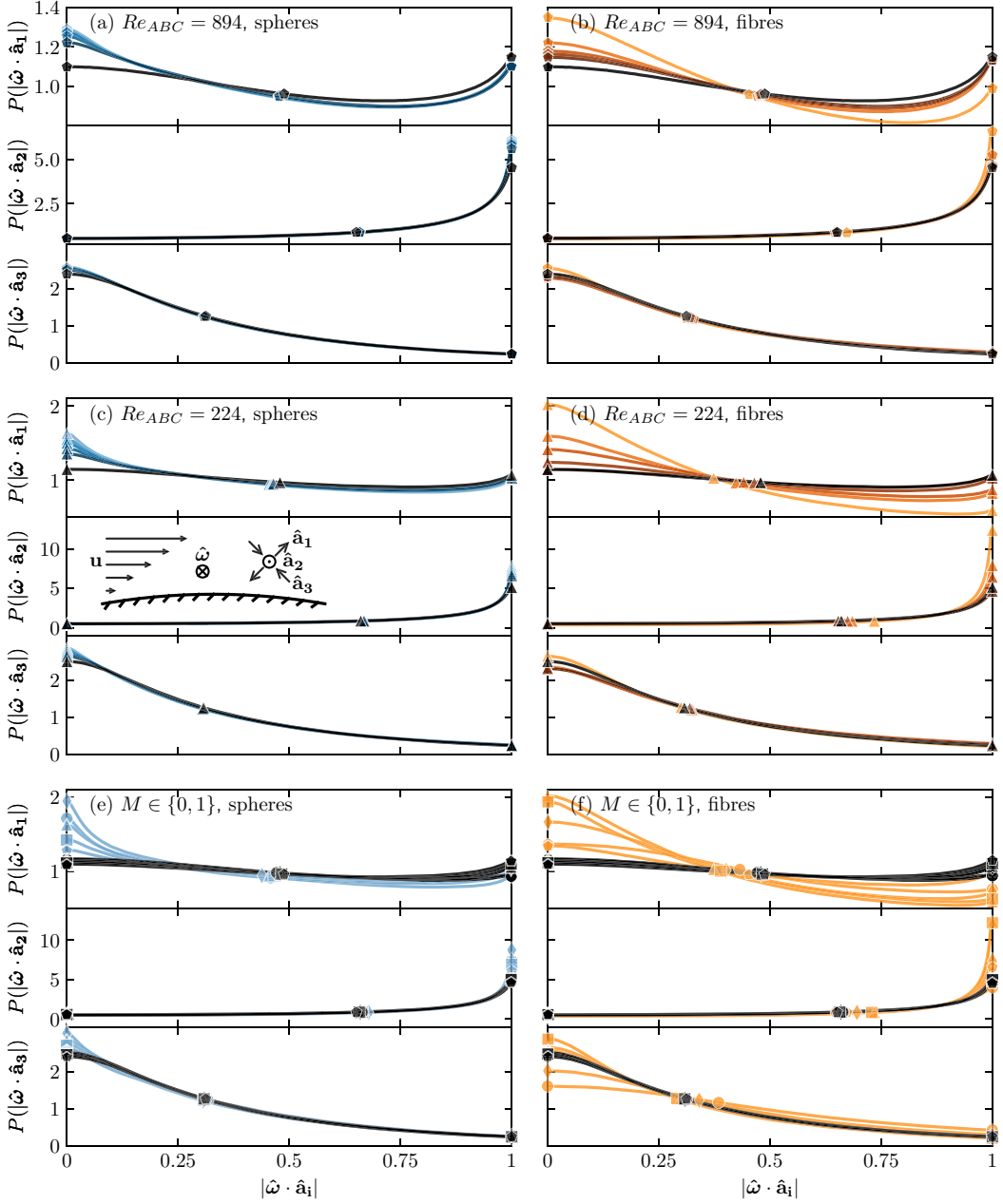


FIG. 10. Histograms of the alignment of the vorticity unit vector  $\hat{\omega}$  with the eigenvectors  $\hat{a}_1$ ,  $\hat{a}_2$ , and  $\hat{a}_3$  of the strain-rate tensor. Flows with spheres are on the left, and flows with fibers are on the right. [(a) and (b)] Cases with  $Re_{ABC} = 894$  for various mass fractions. [(c) and (d)] Cases with  $Re_{ABC} = 224$  for various mass fractions. [(e) and (f)] Fixed ( $M = 1$ ) and single-phase ( $M = 0$ ) cases for various Reynolds numbers. Each case is plotted using its marker, which is listed in Tables I, II, or III. We mark each line at  $|\hat{\omega} \cdot \hat{a}_1| = 0, 1$  and  $\langle |\hat{\omega} \cdot \hat{a}_1| \rangle$ . The inset of panel (c) shows the directions of vorticity and the eigenvectors of the strain rate in a laminar shear flow, where  $\hat{a}_1$  and  $\hat{a}_3$  are confined to the shear plane, while  $\hat{a}_2$  and  $\hat{\omega}$  are perpendicular to it.

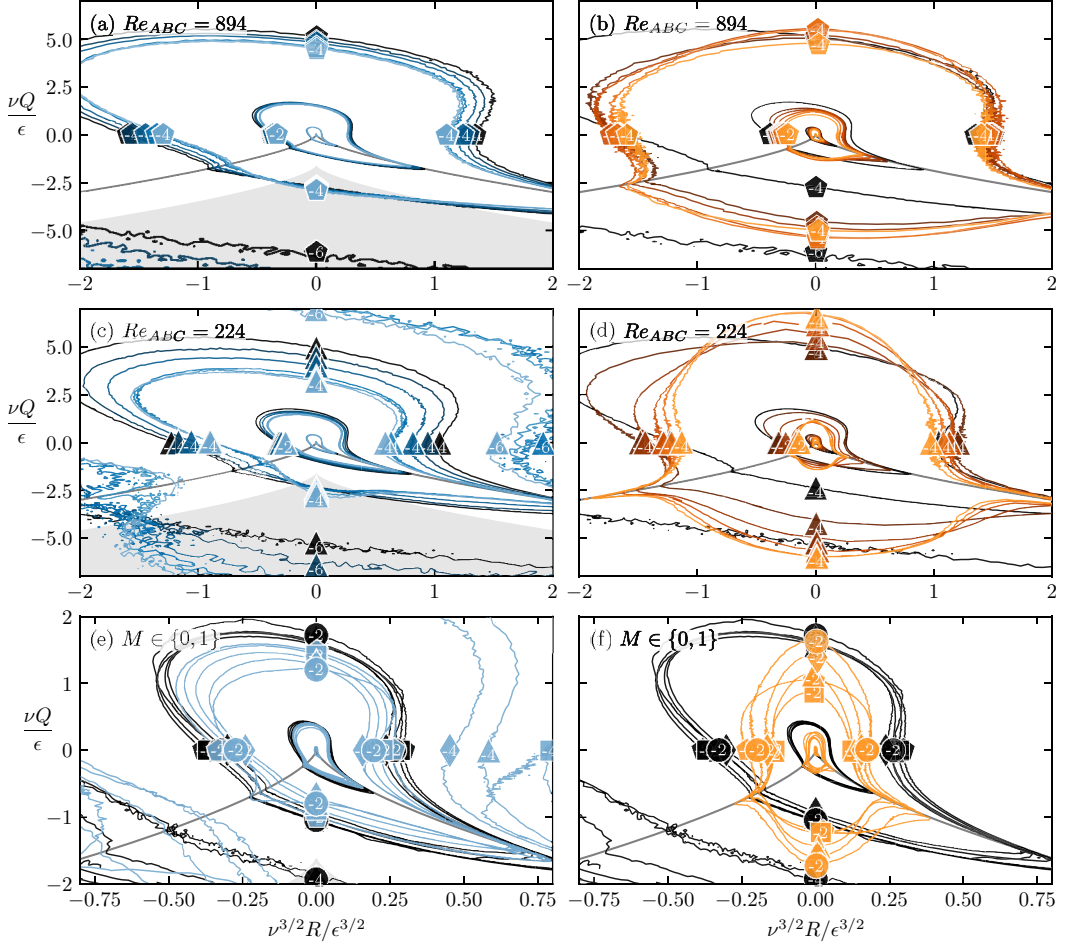


FIG. 11. Joint histograms of the invariants  $Q$  and  $R$  of the fluid velocity gradient tensor. [(a) and (b)] Cases with  $Re_{ABC} = 894$  for various particle mass fractions. [(c) and (d)] Cases with  $Re_{ABC} = 224$  for various particle mass fractions. [(e) and (f)] Fixed ( $M = 1$ ) and single-phase ( $M = 0$ ) cases for various Reynolds numbers. Each case is plotted using its marker, which is listed in Tables I, II, or III. The number on the marker shows the value of  $\log p$  at each contour, where  $p$  is the joint probability density function. The gray curves show where the discriminant is zero [Eq. (18)]. The gray shaded regions in the left panels are the loci of Eq. (19), where we observe an increase  $p$  due to the presence of spheres.

is the balance of the production of vorticity with the production of strain [48]. The eigenvalues  $\Lambda$  of  $\partial_i u_j$  are the roots of the polynomial equation,

$$\Lambda^3 + Q\Lambda + R = 0. \quad (18)$$

Figure 11 shows the joint probability distributions  $p(R, Q)$  for all of our flows. We also plot a line where the discriminant of Eq. (18) is zero:  $27R^2/4 + Q^3 = 0$ . Above this line,  $\partial_i u_j$  has one real and two complex eigenvalues and vortices dominate the flow. Below this line, all three eigenvalues are real, and the flow is dominated by strain. The single-phase distributions have tails in the top-left and bottom-right quadrants; these correspond to stretching vortices and regions where the flow compresses along one axis, respectively [47]. When spheres are added, both  $Q$  and  $R$  are reduced, as the nonslip boundary condition at their surfaces dampens the flow structures. Incidentally, a



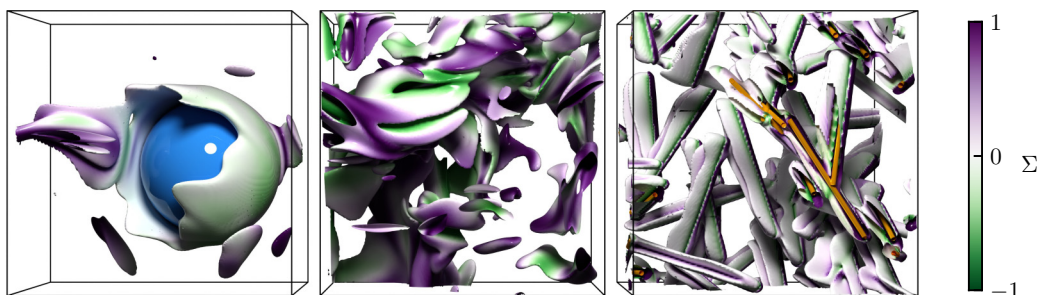


FIG. 12. Surfaces where the dissipation is  $6\epsilon$ , colored according to the value of the flow topology parameter  $\Sigma$ , which distinguishes rotational flow (green), shearing flow (white), and straining flow (purple). We show  $\text{Re}_{\text{ABC}} = 224$  cases with fixed spheres (left), single-phase (center), and fixed fibers (right). The boxes have side length  $L$ .

similar  $Q$  and  $R$  reduction has been seen with droplets [49]. However, we see that the addition of spheres causes  $p(R, Q)$  to increase in the shaded regions in the left panels of Fig. 11. These regions are defined by

$$\frac{27R^2}{4} + Q^3 < -\frac{4\epsilon^3}{v^3}. \quad (19)$$

These shaded regions correspond to a strain-dominated flow. In fact, for pure strain, we have  $Q = -s_{ij}s_{ij}/2$  and  $R = 0$ . Hence we can substitute for  $Q$  and  $R$  in Eq. (19) to estimate that the dissipation is

$$2\nu s_{ij}s_{ij} = -4\nu Q < 4^{4/3}\epsilon \approx 6\epsilon \quad (20)$$

in the straining flow. That is, the dissipation in regions around the spheres is roughly six times greater than the mean dissipation. Fibers also create straining regions in the flow, seen by the increased probability density functions in the lower parts ( $27R^2/4 + Q^3 < 0$ ) of the right-hand panels in Fig. 11. As the fiber mass fraction is increased, the variance of  $R$  is reduced, showing the production of strain and vorticity is suppressed by the fibers. At high fiber mass fractions the distributions are approximately symmetrical in  $R$ , in other words,  $Q$  and  $R$  are uncorrelated (much like the decorrelation of vorticity and strain observed for fiber-laden flows in Fig. 10). This suggests that the small fiber diameter produces many small-scale structures which disrupt the typical turbulent flow. For both particle types, increasing the Reynolds number  $\text{Re}_{\text{ABC}}$  reduces the effect of the particles.

In Fig. 12 we visualize isosurfaces where the local fluid dissipation is six times its bulk value, i.e., where  $2\nu s_{ij}s_{ij} = 6\epsilon$ . As predicted by Eq. (20), the dissipation is greater than  $6\epsilon$  in the near-particle regions. And in keeping with our measurements of the fractal dimension of the dissipation field (Fig. 9), the high-dissipation region near the sphere is approximately sheetlike and two dimensional, while the high-dissipation regions near the fibers are approximately tubelike and one dimensional. In both cases, wakes extend behind the particles, which contribute to the fractal dimension of the dissipation fields. We see the single-phase dissipation structures take various shapes and sizes, giving rise to the multifractal behavior discussed above. In Fig. 12 we color the dissipation isosurfaces according to the local value of the flow topology parameter [50],

$$\Sigma \equiv \frac{2s_{ij}s_{ij} - \omega_i\omega_i}{2s_{ij}s_{ij} + \omega_i\omega_i}, \quad (21)$$

which is essentially the second invariant of the velocity gradient tensor  $Q$  normalized so that it is bounded between  $-1$  and  $1$ . Regions where  $\Sigma = -1$  (green) correspond to pure rotational

flow, regions where  $\Sigma = 0$  (white) correspond to pure shear, and regions where  $\Sigma = 1$  (purple) correspond to pure straining flow. From Fig. 12 we see fibers produce straining flow on the upstream side, and shearing flow in wakes on the downstream side, and this manifests in Fig. 11 as an increase in the spread of  $Q$  for the fiber-laden flows. At the surface of the sphere we see a mostly shearing flow, which supports our observations of strong shear-vorticity alignment ( $|\hat{\omega} \cdot \hat{\mathbf{a}}_2| = 1$ ) in Fig. 10.

#### IV. CONCLUSION

We made simulations of finite-size isotropically and anisotropically shaped particles (spheres and fibers with size  $c$  within the inertial range of scales) in turbulence at various Reynolds numbers and solid mass fractions. We used bulk flow statistics to show that particles reduce turbulence intensity relative to the single-phase case at all Reynolds numbers, with the fibers producing a more significant reduction effect than the spheres. Regarding the trend in anomalous dissipation with Reynolds number, we see that the particle-laden flows tend to behave like single-phase flows as  $\text{Re}_\lambda \rightarrow \infty$ , and the value of anomalous dissipation is  $\epsilon \mathcal{L} / u_{\text{rms}}^3 \approx 0.4$  for both single-phase and particle-laden flows. We see that spheres slow the convergence rate to the anomalous value, and fibers slow it further. Next, we analyzed the flow at each scale of the simulation. Spheres and fibers provide a “spectral shortcut” to the flow, removing energy from the largest scales and injecting it at smaller scales. Spheres’ effect is mainly limited to the large scales, and they provide a spectral shortcut down to the length scale of their diameter. Fibers’ effect, on the other hand, occurs down to the scale of the fiber thickness, even at low Reynolds numbers when it is deep in the viscous range ( $d < \eta$ ). This shortcut of energy to the dissipative scales slows the dissipation’s convergence to its anomalous value as  $\text{Re}_\lambda \rightarrow \infty$ . Our scale-by-scale analysis also showed that particles cause the velocity field to become more intermittent in space. Multifractal spectra of the near-particle dissipation show that spheres enhance dissipation in two-dimensional sheets, and fibers enhance the dissipation in structures with a dimension greater than one and less than two. These lower-dimensional structures are a possible source of intermittency in the flow. Zooming in closer to the flow, we looked at the shape of flow structures using their vorticity and shear. We saw that the particles enhance local shear, spheres suppress vortical flow structures, and fibers produce intense vortical and shearing structures, which overcome the usual vortex stretching behavior. As Reynolds number increases, the flow structures created by the particles become less significant relative to the background turbulence.

To reiterate and answer our questions from Sec. I: *At what Reynolds numbers does turbulence modulation emerge?* We see turbulence modulation at the lowest Reynolds number investigated ( $\text{Re}_\lambda = 12.8$ ). This gives us reason to believe that particles modulate turbulence in even the most weakly turbulent flows ( $\text{Re}_\lambda \rightarrow 0$ ). Second, *does the modulation effect persist as  $\text{Re} \rightarrow \infty$ ?* The values of normalized dissipation and many other statistics presented here do indeed converge on the single-phase result as  $\text{Re} \rightarrow \infty$ . However, the modulation of turbulent kinetic energy  $K'$  appears to have little to no dependence on the Reynolds number. Larger Reynolds numbers must be investigated to test whether the attenuation of  $K'$  goes to zero as  $\text{Re}_{\text{ABC}} \rightarrow \infty$ . Finally, *how do the particle’s characteristic lengths impact the scales of the turbulent flow?* Both spheres and fibers take energy from the flow at scales larger than their size. Spheres reinject energy around the characteristic length of their diameter  $c$ , leaving the smaller scales relatively unperturbed. Indeed, the effect of the spheres on the local flow structures tends to zero as the ratio  $c/\eta$  increases. In contrast, fibers reinject energy around the characteristic length of their thickness  $d$ . The fiber thickness is at a small scale, so local flow structures are disrupted. None of the flow statistics shows any particular discerning feature at the length scale  $c$  of the fibers.

These results relate to various environmental particle-laden flows, such as microplastics in the ocean, volcanic ash clouds, and sandstorms. We have explored the two extremes of isotropic and anisotropic particles, but further work is needed to investigate how intermediate aspect ratio particles such as ellipsoids interact with turbulent flows.

## ACKNOWLEDGMENTS

The research was supported by the Okinawa Institute of Science and Technology Graduate University (OIST) with subsidy funding from the Cabinet Office, Government of Japan. The authors acknowledge the computer time provided by the Scientific Computing & Data Analysis section of the Core Facilities at OIST and the computational resources of the supercomputer Fugaku provided by RIKEN through the HPCI System Research Project (Project IDs: hp210229 and hp210269). S.O. acknowledges the support of Grants No. FJC2021-047652-I and No. PID2022-142135NA-I00 by AEI/MCIN/10.13039/501100011033 and European Union NextGenerationEU/PRTR. I.C. would like to thank Rahul Kumar Singh (OIST) for patient and illuminating discussions of multifractality in turbulence.

The data are available in Ref. [51]

- 
- [1] L. F. Richardson and D. Proctor, Diffusion over distances ranging from 3 km. to 86 km, *Q. J. R. Meteorolog. Soc.* **53**, 149 (1927).
  - [2] J. Westerweel, G. E. Elsinga, and R. J. Adrian, Particle image velocimetry for complex and turbulent flows, *Annu. Rev. Fluid Mech.* **45**, 409 (2013).
  - [3] S. Brizzolara, M. E. Rosti, S. Olivieri, L. Brandt, M. Holzner, and A. Mazzino, Fiber tracking velocimetry for two-point statistics of turbulence, *Phys. Rev. X* **11**, 031060 (2021).
  - [4] R. Monchaux, Measuring concentration with Voronoï diagrams: The study of possible biases, *New J. Phys.* **14**, 095013 (2012).
  - [5] S. Goto and J. C. Vassilicos, Sweep-stick mechanism of heavy particle clustering in fluid turbulence, *Phys. Rev. Lett.* **100**, 054503 (2008).
  - [6] A. Chiarini, I. Cannon, and M. E. Rosti, Anisotropic mean flow enhancement and anomalous transport of finite-size spherical particles in turbulent flows, *Phys. Rev. Lett.* **132**, 054005 (2024).
  - [7] P. J. Ireland, A. D. Bragg, and L. R. Collins, The effect of Reynolds number on inertial particle dynamics in isotropic turbulence. Part 1. Simulations without gravitational effects, *J. Fluid Mech.* **796**, 617 (2016).
  - [8] L. H. Zhao, H. I. Andersson, and J. J. J. Gillissen, Turbulence modulation and drag reduction by spherical particles, *Phys. Fluids* **22**, 081702 (2010).
  - [9] J. Capeceelatro, O. Desjardins, and R. O. Fox, On fluid–particle dynamics in fully developed cluster-induced turbulence, *J. Fluid Mech.* **780**, 578 (2015).
  - [10] S. Olivieri, I. Cannon, and M. E. Rosti, The effect of particle anisotropy on the modulation of turbulent flows, *J. Fluid Mech.* **950**, R2 (2022).
  - [11] L. Brandt and F. Coletti, Particle-laden turbulence: Progress and perspectives, *Annu. Rev. Fluid Mech.* **54**, 159 (2021).
  - [12] G. A. Voth and A. Soldati, Anisotropic particles in turbulence, *Annu. Rev. Fluid Mech.* **49**, 249 (2017).
  - [13] H. Wadell, Volume, shape, and Roundness of rock particles, *J. Geol.* **40**, 443 (1932).
  - [14] L. Zhao, N. R. Challabotla, H. I. Andersson, and E. A. Variano, Rotation of nonspherical particles in turbulent channel flow, *Phys. Rev. Lett.* **115**, 244501 (2015).
  - [15] M. N. Ardekani, P. Costa, W.-P. Breugem, F. Picano, and L. Brandt, Drag reduction in turbulent channel flow laden with finite-size oblate spheroids, *J. Fluid Mech.* **816**, 43 (2017).
  - [16] A. Yousefi, M. N. Ardekani, and L. Brandt, Modulation of turbulence by finite-size particles in statistically steady-state homogeneous shear turbulence, *J. Fluid Mech.* **899**, A19 (2020).
  - [17] J. S. Paschkewitz, Y. Dubief, C. D. Dimitropoulos, E. S. G. Shaqfeh, and P. Moin, Numerical simulation of turbulent drag reduction using rigid fibres, *J. Fluid Mech.* **518**, 281 (2004).
  - [18] J. J. J. Gillissen, B. J. Boersma, P. H. Mortensen, and H. I. Andersson, Fibre-induced drag reduction, *J. Fluid Mech.* **602**, 209 (2008).

- [19] F. Lucci, A. Ferrante, and S. Elghobashi, Modulation of isotropic turbulence by particles of Taylor length-scale size, *J. Fluid Mech.* **650**, 5 (2010).
- [20] S. Oka and S. Goto, Attenuation of turbulence in a periodic cube by finite-size spherical solid particles, *J. Fluid Mech.* **949**, A45 (2022).
- [21] J. Shen, C. Peng, J. Wu, K. L. Chong, Z. Lu, and L.-P. Wang, Turbulence modulation by finite-size particles of different diameters and particle–fluid density ratios in homogeneous isotropic turbulence, *J. Turbul.* **23**, 433 (2022).
- [22] C. Peng, Q. Sun, and L.-P. Wang, Parameterization of turbulence modulation by finite-size solid particles in forced homogeneous isotropic turbulence, *J. Fluid Mech.* **963**, A6 (2023).
- [23] A. Libin and G. Sivashinsky, Long wavelength instability of the ABC-flows, *Q. Appl. Math.* **48**, 611 (1990).
- [24] O. Podvigina and A. Pouquet, On the non-linear stability of the 1:1:1 ABC flow, *Physica D* **75**, 471 (1994).
- [25] J. Kim and P. Moin, Application of a fractional-step method to incompressible Navier-Stokes equations, *J. Comput. Phys.* **59**, 308 (1985).
- [26] See <https://groups.oist.jp/cffu/code> for validations of the code.
- [27] N. Hori, M. E. Rosti, and S. Takagi, An Eulerian-based immersed boundary method for particle suspensions with implicit lubrication model, *Comput. Fluids* **236**, 105278 (2022).
- [28] W.-X. Huang, S. J. Shin, and H. J. Sung, Simulation of flexible filaments in a uniform flow by the immersed boundary method, *J. Comput. Phys.* **226**, 2206 (2007).
- [29] A. Alizad Banaei, M. E. Rosti, and L. Brandt, Numerical study of filament suspensions at finite inertia, *J. Fluid Mech.* **882**, A5 (2020).
- [30] S. Olivieri, L. Brandt, M. E. Rosti, and A. Mazzino, Dispersed fibers change the classical energy budget of turbulence via nonlocal transfer, *Phys. Rev. Lett.* **125**, 114501 (2020).
- [31] Z. Yu, A DLM/FD method for fluid/flexible-body interactions, *J. Comput. Phys.* **207**, 1 (2005).
- [32] B. Snook, E. Guazzelli, and J. E. Butler, Vorticity alignment of rigid fibers in an oscillatory shear flow: Role of confinement, *Phys. Fluids* **24**, 121702 (2012).
- [33] A. Pinelli, I. Z. Naqavi, U. Piomelli, and J. Favier, Immersed-boundary methods for general finite-difference and finite-volume Navier–Stokes solvers, *J. Comput. Phys.* **229**, 9073 (2010).
- [34] S. Shaik and R. Van Hout, Kinematics of rigid fibers in a turbulent channel flow, *Int. J. Multiphase Flow* **158**, 104262 (2023).
- [35] G. I. Taylor, Statistical theory of turbulence, *Proc. R. Soc. Lond. Ser. A* **151**, 421 (1935).
- [36] D. A. Donzis, K. R. Sreenivasan, and P. K. Yeung, Scalar dissipation rate and dissipative anomaly in isotropic turbulence, *J. Fluid Mech.* **532**, 199 (2005).
- [37] C. R. Doering and C. Foias, Energy dissipation in body-forced turbulence, *J. Fluid Mech.* **467**, 289 (2002).
- [38] M. S. Abdelgawad, I. Cannon, and M. E. Rosti, Scaling and intermittency in turbulent flows of elastoviscoplastic fluids, *Nat. Phys.* **19**, 1059 (2023).
- [39] J. Finnigan, Turbulence in plant canopies, *Annu. Rev. Fluid Mech.* **32**, 519 (2000).
- [40] A. N. Kolmogorov, The local structure of turbulence in incompressible viscous fluid for very large Reynolds numbers, *Doklady Akademii Nauk SSSR* **30**, 301 (1941).
- [41] S. B. Pope, *Turbulent Flows* (Cambridge University Press, Cambridge, UK, 2000).
- [42] U. Frisch, *Turbulence: The Legacy of A. N. Kolmogorov* (Cambridge University Press, Cambridge, UK, 1995).
- [43] C. Meneveau and K. R. Sreenivasan, The multifractal nature of turbulent energy dissipation, *J. Fluid Mech.* **224**, 429 (1991).
- [44] S. Mukherjee, S. D. Murugan, R. Mukherjee, and S. S. Ray, Turbulent flows are not *uniformly* multifractal, *Phys. Rev. Lett.* **132**, 184002 (2024).
- [45] Wm. T. Ashurst, A. R. Kerstein, R. M. Kerr, and C. H. Gibson, Alignment of vorticity and scalar gradient with strain rate in simulated Navier–Stokes turbulence, *Phys. Fluids* **30**, 2343 (1987).

- [46] S. Olivieri, A. Mazzino, and M. E. Rosti, On the fully coupled dynamics of flexible fibres dispersed in modulated turbulence, *J. Fluid Mech.* **946**, A34 (2022).
- [47] W. Cheng, *Study of the velocity gradient tensor in turbulent flow*, Ph.D thesis. Stanford University. SUDAAR 685, 1996.
- [48] I. Paul, B. Fraga, M. S. Dodd, and C. C. K. Lai, The role of breakup and coalescence in fine-scale bubble-induced turbulence. II. Kinematics, *Phys. Fluids* **34**, 083322 (2022).
- [49] P. Perlekar, Kinetic energy spectra and flux in turbulent phase-separating symmetric binary-fluid mixtures, *J. Fluid Mech.* **873**, 459 (2019).
- [50] J. Hunt and N. Kevlahan, Rapid Distortion Theory and the structure of turbulence, in *New Approaches and Concepts in Turbulence*, Monte Verità, edited by T. Dracos and A. Tsinober (Birkhäuser, Basel, 1993), pp. 285–316.
- [51] <https://groups.oist.jp/cffu/cannon2024prf>